Wave–Structure Interactions of Flexible Bags with Elastic Tendons: Application to Wave Energy Conversion

Wave-Structure Interactions of Flexible Bags with Elastic Tendons

Adi Kurniawan[1], Scott Brown[2], David Forehand[3], and Hugh Wolgamot[4]

[1]Wave Energy Research Centre, The University of Western Australia, 35 Stirling Terrace, Albany WA 6330, Australia. Email: adi.kurniawan@uwa.edu.au

[2]School of Engineering, Computing and Mathematics, University of Plymouth, Drake Circus, Plymouth, PL4 8AA, United Kingdom

[3]School of Engineering, The University of Edinburgh, Edinburgh, EH9 3JL, United Kingdom

[4]Oceans Graduate School, The University of Western Australia, 35 Stirling Highway, Perth WA 6009, Australia

ABSTRACT

A new type of wave energy device has recently been proposed with the key component being a flexible air-filled bag, which is constructed such that the fabric is encased by an array of tendons. The behaviour of the bag in still water under hydrostatic loading and its dynamic response when subjected to hydrodynamic loading in waves were previously analysed using a numerical model developed with the assumption of inextensible tendons. In the present work, the model is extended to include the effects of tendon elasticity. The behaviour of the bag with tendons of various moduli of elasticity is then compared with that of the bag with inextensible tendons. It is found that adding elasticity to the tendons has a similar effect to that of increasing the air volume connected to the bag, that is, it increases the resonance period of the device. Consequently, a bag with elastic tendons can be made even smaller in size than a bag with inextensible tendons in order to match the same target resonance period.

INTRODUCTION

There are potential advantages in using a flexible deformable body as part of a wave energy device. A flexible device deforms as it oscillates in water, giving rise to a lower hydrostatic stiffness

and thus a longer natural period than those of a rigid body of the same size. This allows the size of the flexible device to be reduced in order to achieve a particular resonance period and, hence, leads to potential savings in material costs. Flexibility also allows such a device to be tuned to different environmental conditions through a change in its mean shape, making it much more adaptable than a rigid device. Transportation of the device is also potentially simpler and cheaper, since the device can assume its mean shape on-site. Furthermore, a flexible device is expected to be more resilient to wave impact, enhancing its survivability in extreme conditions.

This paper considers a recently proposed wave energy device topology in the form of a completely sealed system consisting of a flexible air-filled bag connected to a rigid-walled secondary volume. In the variant that will be discussed here, the device is freely floating and the bag is surface-piercing (see Fig. 1). As the device heaves in waves, the flexible bag expands and contracts, forcing two-way exchange of air with the secondary volume. This drives a turbine located between the two volumes, which acts as a power take-off (PTO). Other variants have also been considered recently, including a freely floating device with a completely submerged bag (Kurniawan et al. 2017b; Farley 2018) and a bottom-mounted device with either a surface-piercing or a completely submerged bag (Kurniawan and Greaves 2016).

The bag is constructed from a fabric encased by an array of meridional tendons. When inflated, the fabric forms lobes between the tendons, thus minimising the tension in the fabric while the tendons become the primary load-carrying elements. The construction is therefore similar to that used in parachutes (Taylor 1963), underwater lifting bags, super-pressure balloons (Cathey 2009), and a recently proposed underwater compressed air energy storage system (Pimm et al. 2014).

The dynamics of the bag as the device oscillates in water is of interest and has previously been analysed assuming that the tendons are inextensible (Kurniawan et al. 2017a). Good agreement was obtained between the numerically predicted response and physical measurements collected from scaled model tests using bags with relatively stiff tendons, validating the modelling approach.

The aim of the present study is to extend this approach to include the effects of tendon elasticity. Like the previous model, the present model, which will be described in the next section, is linear.

As such, the tendons are assumed to obey Hooke's law, whereby the strain of the tendons is linearly proportional to the applied stress. By simulating tendons of various moduli of elasticity, the impacts of tendon elasticity on the behaviour of the bag and its performance as a wave energy device will then be assessed.

NUMERICAL MODEL

Static Shape Calculation

In contrast to a rigid body, which has a fixed shape, a flexible bag containing a certain amount of air and ballasted at the bottom will deform as soon as it is immersed in water. The static or equilibrium shape of the bag in still water is uniquely determined by the internal pressure and submergence of the bottom of the bag. The method to determine the static shape of the bag follows that of Chaplin et al. (2015a) and is based on three assumptions: (1) the bag is axisymmetric, making it sufficient to consider a single tendon; (2) the tension is carried entirely by the tendons whereas there is no tension in the fabric; (3) the tendons are massless for simplicity.

In summary, the process involves discretising the tendon into N arc elements with known lengths but unknown radii of curvature. The radius of curvature of each element is obtained by satisfying the force equilibrium normal to the element, progressing element by element from the top of the bag to the bottom. As the tendon tension and the top elevation are not known beforehand, an iterative process is necessary to obtain the correct tension and elevation.

A cylindrical coordinate system (R, θ, Z) is introduced, where $Z = 0$ is the mean free surface and positive Z points upwards, with the Z-axis coincident with the vertical axis of the bag. The tendon is discretized into N elements of uniform arc length h, related to its radius of curvature ρ_n through the relationship

$$h = -2\rho_n\phi_n, \tag{1}$$

where $2\phi_n = \delta A_n$ is the arc sector angle (see Fig. 2). The radius of curvature is defined to be positive when the element is bulging outwards. The difference in radial and vertical coordinates

between the ends of the element can then be expressed as

$$\delta R_n = (h/\phi_n) \sin \phi_n \cos(A_n + \phi_n), \tag{2}$$

$$\delta Z_n = (h/\phi_n) \sin \phi_n \sin(A_n + \phi_n), \tag{3}$$

where h is the arc length of the element including extension. This is calculated using Hooke's law:

$$h = h_0 \left(1 + \frac{T}{EA}\right), \tag{4}$$

where T is the sum of tension in all the tendons, A is the combined cross-sectional area of the tendons, E is the modulus of elasticity of the tendon, and h_0 is the original length of the tendon before extension. Obviously, $h \to h_0$ as $E \to \infty$.

For given internal pressure and submergence of the bag, the procedure begins by making initial guesses for the tension T and the vertical coordinate at the top of the bag, Z_1. The value of h is determined using Eq. (4). Starting from the top of the bag with a first approximation of $\phi_1 \approx 0$ and working down the tendon, the radius of curvature for each element is calculated using the balance of normal forces

$$\rho_n = \frac{T}{2\pi(P + H_{n+0.5}\rho g Z_{n+0.5})R_{n+0.5}}, \tag{5}$$

where the subscript $n + 0.5$ denotes the value at the midpoint of element n,

$$H_{n+0.5} = \begin{cases} 1, & \text{if } Z_{n+0.5} < 0 \\ 0, & \text{if } Z_{n+0.5} \geq 0, \end{cases} \tag{6}$$

P is the internal bag pressure (relative to atmospheric), ρ is the water density, and g is the acceleration due to gravity.

Once the radius of curvature is known for an element, the angle ϕ_n can be evaluated from Eq. (1), allowing a better approximation for δR_n and δZ_n to be obtained using Eqs. (2) and (3). These are then used to obtain better approximations for $R_{n+0.5}$, $Z_{n+0.5}$, ρ_n, and ϕ_n, which are again

applied in Eqs. (2) and (3) to get the final values of δR_n and δZ_n. The procedure then moves down the tendon to the next element and the above process repeats until the bottom of the bag is reached.

A simple iterative procedure varies the starting values of T and Z_1 until the last node (R_{N+1}, Z_{N+1}) is at the specified radius and submergence to within a small tolerance. For each value of tension, the length of the element is recalculated using Eq. (4).

Dynamic Model

For the dynamic model, a new set of nodes centred at the elements' midpoints is defined, following the approach of Kurniawan et al. (2017a). In the static shape calculation above, these midpoint nodes are denoted as $n + 0.5$, for $n = 1, \ldots, N$, whereas now they are denoted as $n = 2, \ldots, N'$, where $N' = N + 1$.

The balance of static forces normal to each of these new nodes can be written as

$$2\pi h(P + H_n \rho g Z_n) R_n = T(A_{n-1} - A_n), \quad \text{for } n = 2, \ldots, N', \tag{7}$$

which is equivalent to Eq. (5), where Eq. (1) has been used to express the radius of curvature of the element in terms of the angles A_{n-1} and A_n. Together with the top ($n = 1$) and bottom ($n = N' + 1$) nodes, there are in total $N' + 1 = N + 2$ nodes.

For simplicity, only heave and radial motions of the bag will be considered. By expanding the static equation (7) to include time-harmonic motions of small amplitudes about the mean or static position and keeping first-order terms, a set of linearised equations for the dynamic response of node $n = 2, \ldots, N'$ is obtained as

$$2\pi h \left\{ (P + H_n \rho g Z_n) \left(r_n + R_n \frac{\tau}{T + EA} \right) + \left[p + H_n \rho g (z_n + \xi_3) - p_n^{\mathrm{h}} \right] R_n \right\} = T(a_{n-1} - a_n) + \tau(A_{n-1} - A_n), \tag{8}$$

where r_n is the radial displacement of node n, τ is the change in the total tendon tension, p is the pressure change in the bag, ξ_3 is the vertical displacement of the substructure, z_n is the vertical displacement of node n relative to ξ_3, a_{n-1} and a_n are the angular displacements of the endpoints

of the element, and p_n^{h} is the hydrodynamic pressure on node n. Note that

$$h\frac{\tau}{T+EA} = h_0\frac{\tau}{EA}, \tag{9}$$

in accordance with Eq. (4), and so $h[\tau/(T+EA)]$ is the increase in element length due to τ. For an inelastic tendon, $E \to \infty$, and the terms proportional to $1/(T+EA)$ in Eq. (8) vanish.

For the substructure, the dynamic equation is not affected by the elasticity of the tendons. Therefore,

$$-Ta_{N'}\cos A_{N'} - \tau \sin A_{N'} - \pi R_{N'+1}^2(p+\rho g\xi_3) + f_{\mathrm{B}}^{\mathrm{h}} = -\omega^2 M_{\mathrm{B}}\xi_3, \tag{10}$$

as in the inelastic case (Kurniawan et al. 2017a). Here, $f_{\mathrm{B}}^{\mathrm{h}}$ is the vertical hydrodynamic force on the substructure and M_{B} is the mass of the substructure.

Each of the uppercase quantities in Eqs. (8) and (10), as well as the element length h, is either specified or a solution of the static calculation described earlier, whereas the complex amplitudes p, ξ_3, τ, $f_{\mathrm{B}}^{\mathrm{h}}$, $p_{n|n=2,\ldots,N'}^{\mathrm{h}}$, $r_{n|n=1,\ldots,N'+1}$, $z_{n|n=1,\ldots,N'+1}$, and $a_{n|n=1,\ldots,N'}$ are as yet unknown. Hence, there are $4N'+5$ unknowns in total. Equations (8) and (10) together provide N' equations. In addition, the boundary conditions at the top of the bag are $r_1 = 0$ and $a_1 = 0$, whereas at the bottom, $r_{N'+1} = z_{N'+1} = 0$. These are 4 equations altogether. The remaining $3N'+1$ equations, which will be presented below, are provided through N' equations relating the angular displacements of the elements to the radial displacements of the nodes (Eq. (11)); N' equations relating the vertical displacements to the radial displacements of the nodes (Eq. (12)); N' equations relating the hydrodynamic pressure $p_{n|n=2,\ldots,N'}^{\mathrm{h}}$ and the hydrodynamic force $f_{\mathrm{B}}^{\mathrm{h}}$ to the displacements of the nodes and the substructure (Eqs. (13) and (14)); and one equation relating the dynamic pressure p to the radial and vertical displacements of the nodes (Eq. (15)).

The relationship between the radial and vertical displacements of the nodes, and the angular displacement of the elements can be derived by observing Fig. 3, which is applicable for $n = 2,\ldots,N'-1$. Note that the distance between any two neighbouring nodes at the mean position is h, except for the first two and the last two nodes, where the distance is $h/2$. To first order, the two

sets of equations are

$$a_n(Z_{n+1} - Z_n) = (R_{n+1} - R_n)\frac{\tau}{T + EA} - (r_{n+1} - r_n), \quad \text{for } n = 1, \ldots, N' \tag{11}$$

$$(R_{n+1} - R_n)(r_{n+1} - r_n) + (Z_{n+1} - Z_n)(z_{n+1} - z_n) = \begin{cases} h^2 \frac{\tau}{T+EA}, & \text{for } n = 2, \ldots, N' - 1 \\ \frac{h^2}{4} \frac{\tau}{T+EA}, & \text{for } n = 1 \text{ and } n = N'. \end{cases} \tag{12}$$

The hydrodynamic pressure $p^{\mathrm{h}}_{n|n=2,\ldots,N'}$ on the nodes and the hydrodynamic force $f^{\mathrm{h}}_{\mathrm{B}}$ on the substructure can be expressed as the sum of radiation and excitation parts, where the excitation part is the pressure or force due to the incident wave on the mean geometry of the device, whereas the radiation part is due to the device's own motion in otherwise still water. Thus,

$$p^{\mathrm{h}}_n = \begin{cases} 0, & \text{for } n = 2, \ldots, n_{\mathrm{wl}} - 1 \\ \sum_{k=n_{\mathrm{wl}}}^{N'} (-r_k \sin A_{k-0.5} + z_k \cos A_{k-0.5}) p^{\mathrm{R}}_{n,k} + \xi_3 p^{\mathrm{R}}_{n,3} + p^{\mathrm{exc}}_n, & \text{for } n = n_{\mathrm{wl}}, \ldots, N' \end{cases} \tag{13}$$

$$f^{\mathrm{h}}_{\mathrm{B}} = \sum_{k=n_{\mathrm{wl}}}^{N'} (-r_k \sin A_{k-0.5} + z_k \cos A_{k-0.5}) F^{\mathrm{R}}_{\mathrm{B},k} + \xi_3 F^{\mathrm{R}}_{\mathrm{B},3} + F^{\mathrm{exc}}_{\mathrm{B}}. \tag{14}$$

Here, $n = n_{\mathrm{wl}}$ is the first node below the waterline; $-r_k \sin A_{k-0.5} + z_k \cos A_{k-0.5}$ is the outward displacement of node k in the direction normal to the element; $p^{\mathrm{R}}_{n,k}$ is the pressure on node n due to a unit outward normal displacement of node k; $p^{\mathrm{R}}_{n,3}$ is the pressure on node n due to a unit heave displacement of the mean geometry; p^{exc}_n is the excitation pressure on node n; $F^{\mathrm{R}}_{\mathrm{B},k}$ is the vertical force on the substructure due to a unit normal displacement of node k; $F^{\mathrm{R}}_{\mathrm{B},3}$ is the vertical force on the substructure due to a unit heave displacement of the mean geometry; and $F^{\mathrm{exc}}_{\mathrm{B}}$ is the vertical excitation force on the substructure. The quantities $p^{\mathrm{R}}_{n,k}$, $p^{\mathrm{R}}_{n,3}$, p^{exc}_n, $F^{\mathrm{R}}_{\mathrm{B},k}$, $F^{\mathrm{R}}_{\mathrm{B},3}$, and $F^{\mathrm{exc}}_{\mathrm{B}}$ can be computed using a radiation/diffraction panel method, such as WAMIT (WAMIT 2016) or Nemoh (Babarit and Delhommeau 2015).

The dynamic pressure p in the bag is related to the nodal displacements through (Kurniawan et al. 2017a)

$$p = -Ev, \tag{15}$$

with

$$\frac{1}{E} = \frac{V_s C}{\gamma(P + P_{atm})C + i\omega M_s} + \frac{V}{\gamma(P + P_{atm})}, \tag{16}$$

$$v = \frac{\pi}{3} \sum_{n=1}^{N'} \left\{ (Z_n - Z_{n+1}) \left[(2R_n + R_{n+1}) r_n + (R_n + 2R_{n+1}) r_{n+1} \right] + (z_n - z_{n+1})(R_n^2 + R_n R_{n+1} + R_{n+1}^2) \right\}. \tag{17}$$

In Eq. (16), V is the mean volume of air connected to the bag (note that V does not necessarily have to be equal to the physical volume of the bag), V_s and M_s are the mean volume and mass of air in the secondary volume, P_{atm} is the atmospheric pressure, γ is the heat capacity ratio, and C is the PTO coefficient, which relates the air mass flow through the PTO and the pressure difference across it:

$$i\omega m_s = -i\omega m = C(p - p_s). \tag{18}$$

The dynamic pressure in the secondary volume is given as (Kurniawan et al. 2017a)

$$p_s = \frac{\gamma(P + P_{atm})C}{\gamma(P + P_{atm})C + i\omega M_s} p. \tag{19}$$

Equation (17) expresses the volume amplitude of the bag v in terms of the radial and vertical displacements of the nodes.

Equation (15) thus completes the system of linear equations for the dynamic model. This system of equations may be expressed in a matrix form and solved using standard methods.

Once the equations are solved, the mean absorbed power can be obtained from

$$\mathcal{P} = \frac{C}{2\rho_{air}} |p - p_s|^2, \tag{20}$$

where ρ_{air} is the mass density of air in the system at the mean pressure P. For convenience, we

may introduce the PTO damping B_{PTO}, defined as

$$B_{\mathrm{PTO}} = \rho_{\mathrm{air}}/C, \tag{21}$$

from which we have an alternative expression for the mean absorbed power:

$$\mathcal{P} = \frac{|p - p_{\mathrm{s}}|^2}{2B_{\mathrm{PTO}}}. \tag{22}$$

STATIC BEHAVIOUR

At equilibrium, the weight of a freely floating body equals its buoyancy. This means that for a given amount of ballast, the submergence and shape of the bag must be such that they give the required buoyancy. For the same amount of ballast, the submergence and shape vary, depending on the amount of air in the bag. Plotting these as a function of the bag pressure gives C-shaped trajectories, as first reported by Chaplin et al. (2015b) for a bag with inextensible tendons.

As an example, let us consider a bag with an initial tendon length of 0.95 m, bottom radius R_{N+1} of 0.07 m, and required buoyancy of 0.1 m^3 of water, that is, we use the same dimensions as used by Kurniawan et al. (2017a) for a model-scale bag. Fig. 4 shows trajectories of the top and bottom elevations of the bag for various values of EA, ranging from 5 kN to 1 GN. The 1 GN case may be considered as inextensible. Each trajectory is obtained by calculating the static shape of the bag for a range of internal pressure and bottom elevation, and finding those shapes which give the required buoyancy. In general, the trajectories are C-shaped, but it may be noticed that they exhibit a reversed curvature along the upper end as elasticity is increased. Each trajectory pair traces the top and bottom elevations of the bag at equilibrium, as the amount of air in the bag is varied. With decreasing amount of air, the internal pressure first decreases until it reaches a minimum, and then increases as the bag sits lower in the water, before it sinks when there is not enough air to keep the bag afloat. Similar trajectories can be plotted for the radius of the bag at the water plane, the total tension in all tendons, and the volume of the bag. These are shown in Fig. 5.

All trajectories in these figures shift to the left as the tendon elasticity is increased. This is

because a bag with more elastic tendons can expand more and thus accommodate more air without as much increase in pressure than a bag with stiffer tendons can, as seen from Fig. 5(c). It is also observed that the behaviour of the bags with various tendon elasticity is more similar to each other when they are almost fully deflated than when they are fully inflated (the trajectories merge into one line). As seen from Fig. 5(b), the total tension in the tendons tends asymptotically to approximately 1 kN with decreasing amount of air, irrespective of the value of EA. This is due to the fact that with decreasing amount of air, all bags will have an increasingly elongated profile in the vertical direction, and thus the tendons will be more vertically aligned. The sum of tension in the tendons will then be approximately equal to the submerged weight of the substructure, which in this case is equal to 100 kgf or 0.981 kN. A similar observation can be made from Fig. 5(c). The volumes of the bags all tend to 0.1 m^3, their required buoyancy, when they are just about to sink.

Fig. 6(a) shows the tendon profiles at the minimum pressures possible with different values of EA. Plotting the top and bottom elevations of the bag against the minimum possible bag pressures for the different values of EA reveals approximately linear relationships between the elevations and the minimum possible pressure, as evident from Fig. 6(b).

DYNAMIC BEHAVIOUR

For the dynamic calculations, it is assumed that the substructure is a cylinder with a hemispherical base (as in Fig. 1 and 8). The cylinder radius is 0.152 m and the cylinder height, excluding the hemisphere, is 0.460 m. The mass of the substructure is 140 kg. The same dimensions were used in the previous study (Kurniawan et al. 2017a). The air density at atmospheric pressure is given as 1.225 kg/m^3, while the heat capacity ratio is taken as 1.4. For the calculation of the hydrodynamic quantities, the water depth is assumed to be 3 m. In the calculations, the tendon is discretised into 40 elements, i.e., $N = 40$.

Four cases are defined having different tendon elasticity but with equilibrium conditions selected such that the bags all have the same waterplane radius of 0.341 m at mean position, to provide an equitable comparison. The cases are defined in Table 1, where the mean bag pressure and bag bottom elevation obtained from the static calculations are given, as well as the calculated mean

bag volume, tendon tension, and element length. A high value of EA is chosen for Case 1 and thus it can be regarded to approximate a bag with inextensible tendons. The mean tendon profiles corresponding to these four cases are shown in Fig. 7.

The volume of air connected to the bag, V, is taken to be equal to the physical volume of the bag. This varies slightly depending on the mean shape of the bag. The secondary air volume, V_s, is kept at 2.268 m^3. Although this is much bigger than the volume of the device at model scale, the corresponding full-scale total volume of air ($V + V_s$) would fit into a full-scale device, due to the scaling effects associated with air compressibility (Chaplin et al. 2015a).

Typical responses of the device are shown in Fig 8, which displays snapshots of the device during one oscillation cycle, when subjected to incident waves of amplitude 0.05 m and various periods (as indicated above each plot). These periods correspond to the periods at which the power function (i.e., the mean absorbed power divided by the incident wave amplitude squared; see Eq. (20) and Eq. (22)) peaks in each case, where the same PTO damping, $B_{\mathrm{PTO}} = 15.58$ kPa m^{-3} s, has been used for all cases.

The response of the device varies depending on the selected PTO damping. To illustrate this, each of the dynamic responses in Fig. 9 is plotted for a range of different PTO damping values. Greater PTO damping (or, smaller PTO coefficient C) corresponds to greater resistance of the flow between the two volumes; cf. Eq. (18). Fig. 9 shows that as the PTO damping is decreased (i.e., the flow resistance is reduced), the peak of the response shifts from left to right, i.e., the device resonates at longer periods. This is because the two volumes increasingly become one volume as the flow resistance is reduced, resulting in a greater compliance of the bag which leads to longer resonance periods. This effect is clearly seen from the plots of the pressure amplitudes, Fig. 9(b), where the pressures in the two volumes become more equal as the flow resistance is reduced. This peak shifting, which results in a double-peaked response envelope, appears to be a characteristic of compressible devices with two air volumes (Kurniawan et al. 2014).

For comparison, the responses of a rigid body having the same geometry as the mean geometry of the bag and absorbing energy through heave relative to a fixed reference (e.g. the sea bed) are

also plotted in Fig. 9(a) and (e). The PTO damping in each case is chosen to maximise the absorbed power at resonance, and they are equal to 81.84, 84.66, 89.49, and 92.46 kg/s for Case 1 to 4. The envelopes of the power function for the rigid body are also shown in Fig. 9(a). Since the mean geometries of the bag are similar, and they have the same waterplane radius and mass, the rigid bodies have similar responses. This, however, is not the case with the flexible bags. The elasticity of the tendons has a clear effect on the dynamic response of the bag, with the more elastic bags resonating at longer periods and with generally higher amplitudes.

As seen from Fig. 9(a), the rigid body has a broader power function envelope due to the fact that it is reacting against a fixed reference. The bandwidth of the flexible bag device is narrower because, firstly, it is a self-reacting device and, secondly, it is deformable. The flexible bag device can however attain higher values of mean absorbed power at the peaks.

The change in tendon element length per incident wave amplitude is plotted in Figure 10 for Cases 1 to 4. The curves in this figure are proportional to the tension amplitude curves in Fig. 9(d) by a factor of EA. With increasing elasticity, there is more stretch in the tendons.

A possible disadvantage of having too high elasticity is the higher strain which may limit the range of wave conditions in which the device is stable. This may be inferred from the static trajectories in Fig. 4, where it is seen that with increasing elasticity, the C-shaped trajectories become more elongated vertically, implying that the device becomes increasingly more sensitive to small variations in the amount of air in the system and thus it would be more difficult to maintain equilibrium.

PERFORMANCE IN AN ACTUAL WAVE CLIMATE

A longer resonance period is beneficial in terms of device economy. Adding elasticity to the tendons increases the resonance period of the body, and therefore allows the device to be made even smaller. In this section, the performance of a full-scale flexible bag device with various tendon elasticity in an actual wave climate is compared. The chosen wave climate is that of the European Marine Energy Centre (EMEC) in Scotland. The joint probability diagram for significant wave height and mean wave period at this location is taken from (Nielsen and Pontes 2010).

The calculation assumes that each sea state is described by the modified Pierson-Moskowitz spectrum (Tucker and Pitt 2001), and, for simplicity, the following approximate relationships between the peak period T_p, mean period T_z, and energy period T_e are assumed (Nielsen and Pontes 2010):

$$T_p = 1.4\,T_z, \tag{23}$$

$$T_e = 1.2\,T_z. \tag{24}$$

For each sea state, the mean absorbed power is calculated as

$$\mathcal{P}(H_s, T_z) = 2\int_0^\infty \frac{\mathcal{P}(\omega)}{|\eta|^2} S(\omega, H_s, T_z)\,\mathrm{d}\omega, \tag{25}$$

where $S(\omega, H_s, T_z)$ is the wave spectrum for the sea state. Two cases are considered. First, the PTO damping is assumed to be constant and optimised to maximise the mean absorbed power for the entire wave climate, which is given as

$$\overline{\mathcal{P}} = \sum_{H_s}\sum_{T_z} \mathcal{P}(H_s, T_z)\,\mathrm{Prob}(H_s, T_z), \tag{26}$$

where $\mathrm{Prob}(H_s, T_z)$ is the long-term probability of occurrence of the sea state. Second, the PTO damping is optimised to maximise the mean absorbed power for each sea state.

The mean absorbed power for the given wave climate is calculated for a number of different scales of the device. From this, the mean capture width ratio can be calculated according to

$$\overline{\mathrm{CWR}} = \overline{\mathcal{P}}/\overline{J}, \tag{27}$$

where

$$\overline{J} = \sum_{H_s}\sum_{T_z} \frac{\rho g^2}{64\pi} T_e H_s^2\,\mathrm{Prob}(H_s, T_z), \tag{28}$$

assuming deep water condition, for simplicity.

The mean capture width ratio $\overline{\text{CWR}}$ as a function of scale is plotted in Fig. 11(a) for the four tendon elasticity cases defined earlier. The mean capture width ratio is seen to increase with scale, in agreement with the observation made by (Babarit 2015). As expected, the device in Case 4 (which has the most elastic tendons) has the highest $\overline{\text{CWR}}$ for a given scale, up to approximately a scale of 30, where the $\overline{\text{CWR}}$ appears to peak. The $\overline{\text{CWR}}$ for devices in Cases 1 to 3 increase further beyond this scale and appear to peak at a larger scale. Using a constant PTO damping for the entire wave climate is seen to produce almost the same performance as using variable PTO damping optimised for each sea state.

The growth of the $\overline{\text{CWR}}$ with scale (up to a saturation point which happens at a relative large scale) makes sense if we consider that the wave energy resource for a particular sea state is proportional to wave period and to the square of the wave height (see Eq. (28)). So, although the most frequently occurring sea states are composed of relatively short waves, the waves with the highest average energy over the entire wave climate are longer. These longer waves therefore have more weighting in the total energy production and, consequently, larger devices are preferred.

For the same wave climate, the mean absorbed power is proportional to the $\overline{\text{CWR}}$ times the scale. If cost were linearly proportional to scale, then the $\overline{\text{CWR}}$ would be a true representation of the device economy, and a device would need to be sized to a scale where the $\overline{\text{CWR}}$ is maximum. At a scale of 30, this would be quite a large device.

A completely different picture is obtained if, instead, the mass of the device is taken as a proxy for cost, as shown in Fig. 11(b), where the ratio of the mean absorbed power to device mass (or ballast mass if the mass of the bag is neglected, as done here) is plotted for the four cases. Again, the device with the highest tendon elasticity has the highest power-to-mass ratio. However, it is more beneficial to have a smaller device, with the power-to-mass ratio peaking at a scale smaller than 10.

Taking the device mass as a proxy for cost is just one among many possibilities. The actual cost of the device may be proportional to $(\text{scale})^2$ or somewhere between $(\text{scale})^1$ and $(\text{scale})^3$, rather than $(\text{scale})^3$, as implied in taking mass as a proxy for cost.

It should be noted that to maximise power absorption, especially for a relatively small device, requires displacement amplitudes that can be exceedingly large. Fig. 12 shows the ratio of the maximum standard deviation of the bag top displacement to the mean freeboard. To attain the absorbed power values shown in Fig. 11 would require a device of a scale smaller than 20 to be completely submerged.

The preceding analysis applies for a passive device without any means for reactive control. A different conclusion may be obtained if reactive control is considered. In addition, the PTO damping has been allowed to assume any value, and no drag has been included in the model.

CONCLUSION

Static and dynamic numerical analyses of a wave energy device incorporating a flexible bag with elastic tendons have been presented. Linear analysis has been employed throughout and only heave and radial displacements have been considered. From the static analysis, it is found that adding elasticity to the tendons lowers the minimum possible pressure in the bag. C-shaped trajectories similar to those of a bag with inextensible tendons are also found with the elastic-tendon bag, but the trajectories are characterised by steeper gradients as the elasticity is increased.

Dynamically, the effect of having elastic tendons is found to be similar to that of having a larger air volume connected to the bag. An elastic-tendon bag has an even longer resonance period than an inextensible-tendon bag for the same waterplane area and the same amount of ballast, offering a greater potential for cost saving. Calculations of the expected absorbed power in an actual wave climate have been performed confirming the benefit, in terms of power production, of having elastic tendons over inextensible tendons.

Varying the PTO damping (i.e., the flow resistance between the two air volumes) shifts the peak response of the flexible bag device across a range of periods, with a resulting double-peaked envelope of the mean absorbed power. The multi-peak envelope is similar to that of a classical self-reacting point absorber composed of two rigid bodies (Falnes 1999). However, whereas the response of the two-body device alternates between single-peaked (when the PTO damping is large) and double-peaked (when the PTO damping is small), the response of the flexible bag device

stays single-peaked but shifts from shorter to longer periods as the PTO damping is reduced. A more detailed comparison with a classical self-reacting point absorber, including calculations of the expected power production in an actual wave climate, is planned for a future study.

ACKNOWLEDGMENTS

Dr. Thanh Toan Tran from the National Renewable Energy Laboratory (NREL) provided the hydrodynamic coefficients for the dynamic response calculations. A.K. is supported by the Wave Energy Research Centre, jointly funded by The University of Western Australia and the Western Australian Government, via the Department of Primary Industries and Regional Development (DPIRD). Part of this study was conducted while A.K. was with the Department of Civil Engineering, Aalborg University. S.B. and D.F would also like to acknowledge support from the Wave Energy Scotland through the project "A feasibility study on Elastomeric-based WECs" (ELASTO).

REFERENCES

Babarit, A. (2015). "A database of capture width ratio of wave energy converters." *Renewable Energy*, 80, 610–628.

Babarit, A. and Delhommeau, G. (2015). "Theoretical and numerical aspects of the open source BEM solver NEMOH." *Proceedings of the 11th European Wave and Tidal Energy Conference (EWTEC2015)*, Nantes, France.

Cathey, H. (2009). "The NASA super pressure balloon – A path to flight." *Advances in Space Research*, 44(1), 23–38.

Chaplin, J., Farley, F., Greaves, D., Hann, M., Kurniawan, A., and Cox, M. (2015a). "Numerical and experimental investigation of wave energy devices with inflated bags." *Proc. 11th Eur. Wave and Tidal Energy Conf. Nantes, France*.

Chaplin, J. R., Farley, F., Kurniawan, A., Greaves, D., and Hann, M. (2015b). "Forced heaving motion of a floating air-filled bag." *Proc. 30th Int. Workshop on Water Waves and Floating Bodies*, Bristol, UK.

Falnes, J. (1999). "Wave-energy conversion through relative motion between two single-mode oscillating bodies." *Journal of Offshore Mechanics and Arctic Engineering*, 121, 32–38.

Farley, F. J. M. (2018). "The underwater resonant airbag: a new wave energy converter." *Proceedings of the Royal Society A: Mathematical, Physical and Engineering Sciences*, 474(2215), 20170192.

Kurniawan, A., Chaplin, J. R., Greaves, D. M., and Hann, M. (2017a). "Wave energy absorption by a floating air bag." *Journal of Fluid Mechanics*, 812, 294–320.

Kurniawan, A., Chaplin, J. R., Hann, M. R., Greaves, D. M., and Farley, F. J. M. (2017b). "Wave energy absorption by a submerged air bag connected to a rigid float." *Proceedings of the Royal Society A: Mathematical, Physical and Engineering Sciences*, 473(2200), 20160861.

Kurniawan, A. and Greaves, D. (2016). "Wave power absorption by a submerged balloon fixed to the sea bed." *IET Renewable Power Generation*, 10, 1461–1467(6).

Kurniawan, A., Greaves, D., and Chaplin, J. (2014). "Wave energy devices with compressible volumes." *Proceedings of the Royal Society of London A*, 470(2172).

Nielsen, K. and Pontes, T. (2010). "Annex II Task 1.1 Generic and site-related wave energy data." *Report No. T02-1.1*, OES IA (September).

Pimm, A. J., Garvey, S. D., and de Jong, M. (2014). "Design and testing of energy bags for underwater compressed air energy storage." *Energy*, 66, 496–508.

Taylor, G. I. (1963). "On the shapes of parachutes." *The Scientific Papers of G. I. Taylor*, G. K. Batchelor, ed., Cambridge University Press, 26–37. (Original work published 1919).

Tucker, M. J. and Pitt, E. G. (2001). *Waves in Ocean Engineering*, Vol. 5 of *Ocean Engineering Series*. Elsevier.

WAMIT (2016). *User Manual*. WAMIT, Inc., Chestnut Hill, MA, <http://www.wamit.com>. Version 7.2.

List of Tables

TABLE 1. Parameters of the selected cases

Case	EA [N]	P [m]	$Z_{N'+1}$ [m]	V [m^3]	T [N]	h [m]
1	1×10^9	0.370	-0.438	0.141	1.375×10^3	2.375×10^{-2}
2	5×10^4	0.328	-0.467	0.142	1.210×10^3	2.432×10^{-2}
3	1×10^4	0.274	-0.547	0.145	0.997×10^3	2.612×10^{-2}
4	5×10^3	0.256	-0.630	0.147	0.927×10^3	2.816×10^{-2}

List of Figures

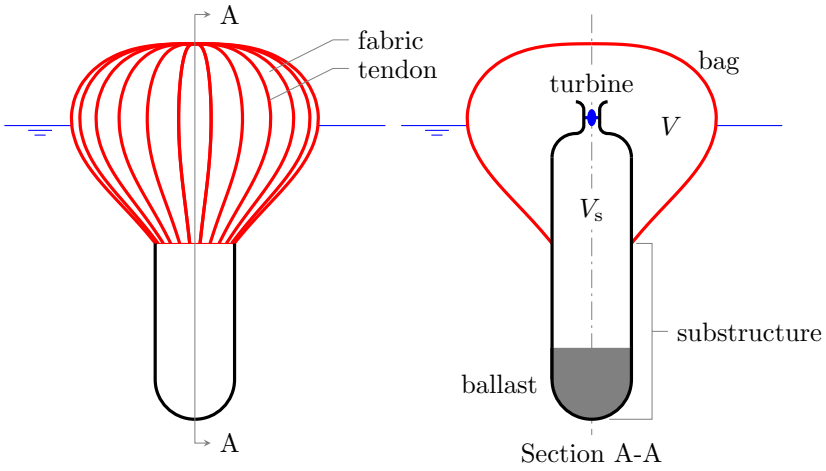

Fig. 1. Sketch of the floating bag device, showing the main components and the two air volumes, V and V_s.

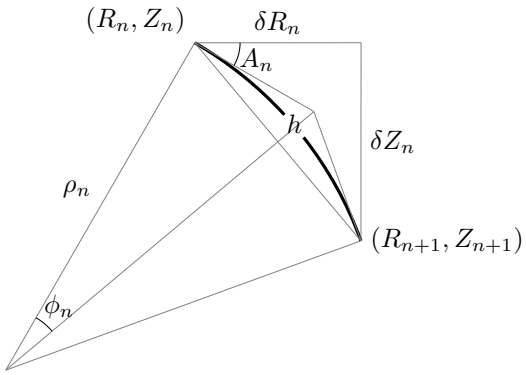

Fig. 2. One arc element.

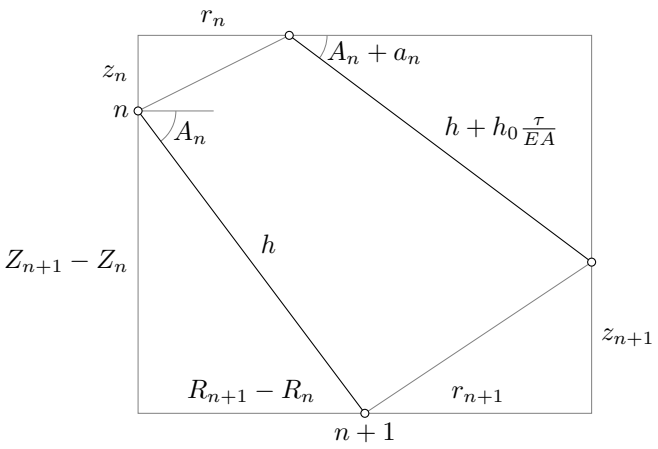

Fig. 3. Positions of two neighbouring nodes before and after displacements.

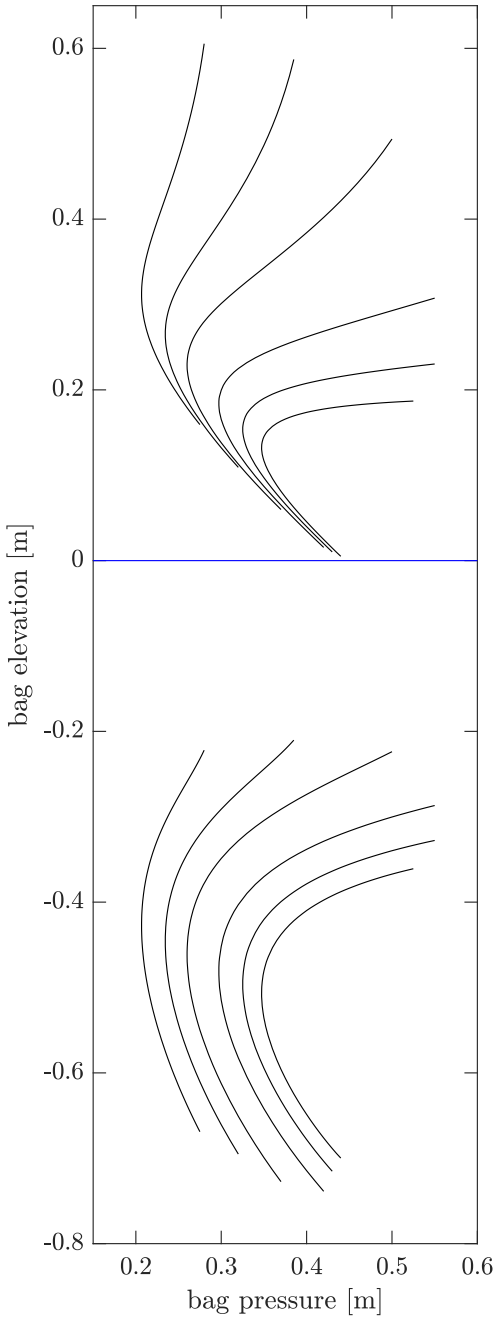

Fig. 4. Trajectories of top and bottom elevations of the bag for various values of EA: from left to right, 5 kN, 7 kN, 10 kN, 20 kN, 50 kN, 1 GN. The bag pressure is measured in terms of the pressure head (i.e., $P/(\rho g)$).

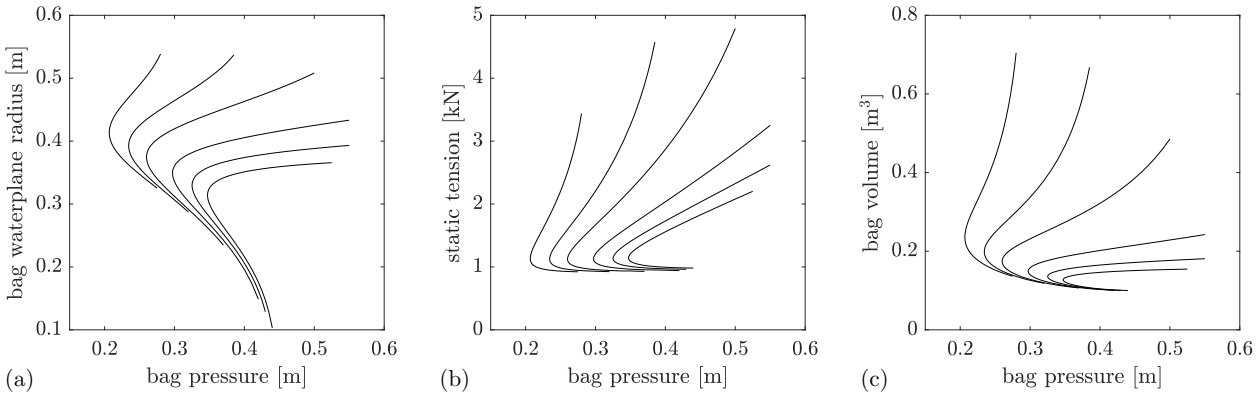

Fig. 5. Trajectories of (a) waterplane radius of the bag, (b) total tendon tension, and (c) bag volume for various values of EA: from left to right, 5 kN, 7 kN, 10 kN, 20 kN, 50 kN, 1 GN.

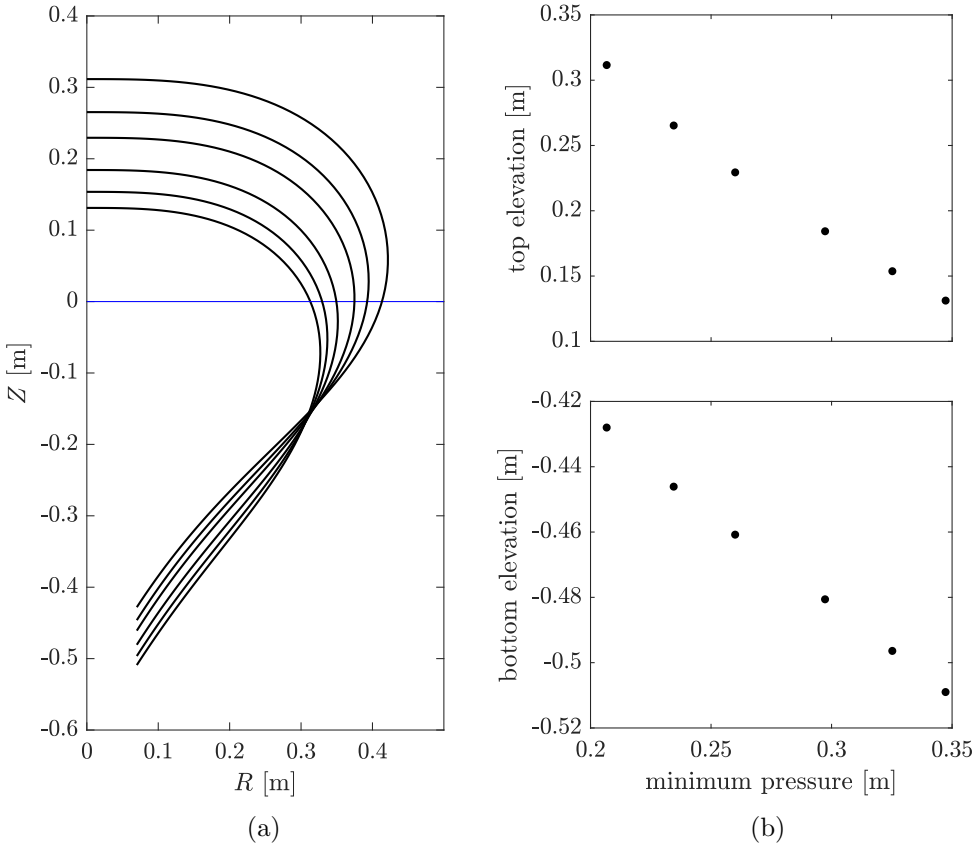

Fig. 6. (a) Tendon profiles at the minimum bag pressures possible with various values of EA: highest profile to lowest profile, 5 kN, 7 kN, 10 kN, 20 kN, 50 kN, 1 GN. (b) Variations of top and bottom elevations of the bag with minimum possible bag pressures for various values of EA.

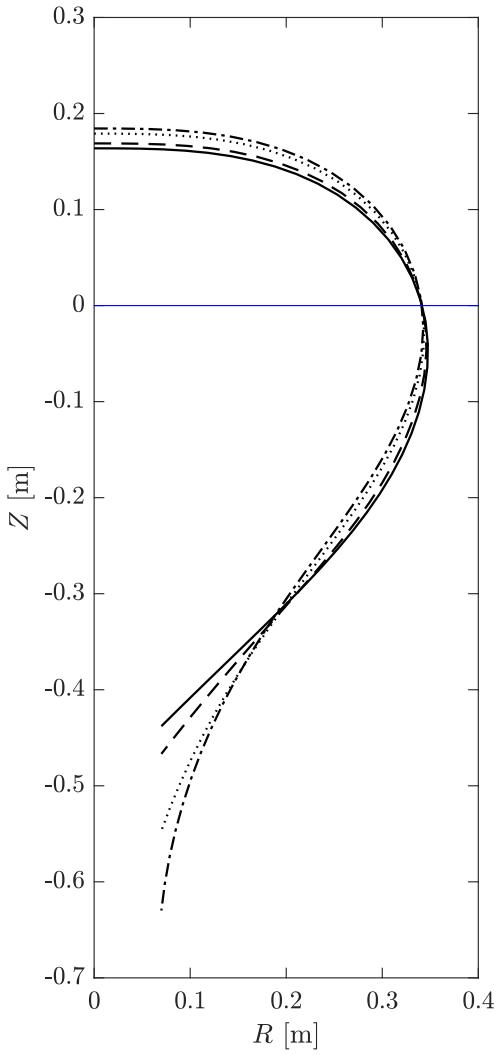

Fig. 7. Mean tendon profiles having the same waterplane radius of 0.341 m: Case 1 (solid), Case 2 (dashed), Case 3 (dotted), and Case 4 (dash-dotted).

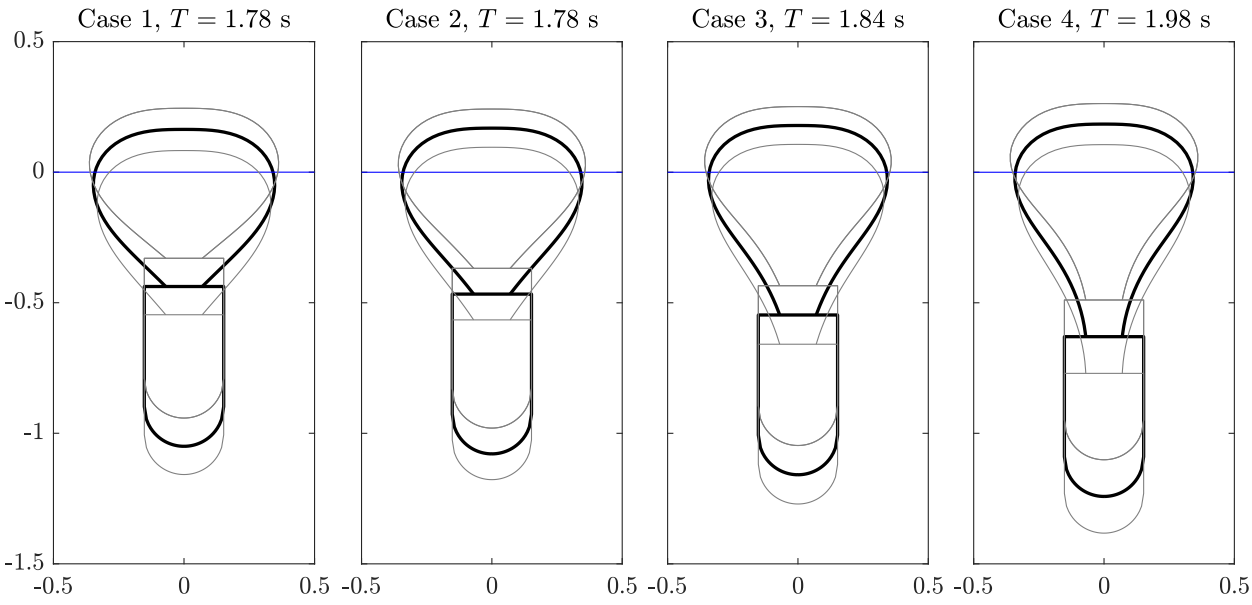

Fig. 8. Snapshots of the device at mean position (thick line) and when the top of the bag is at its highest and lowest elevations (thin lines). The oscillations are in response to incident waves of amplitude 0.05 m and with periods as indicated. The PTO damping, $B_{\mathrm{PTO}} = 15.58$ kPa m^{-3} s, is kept constant in all cases.

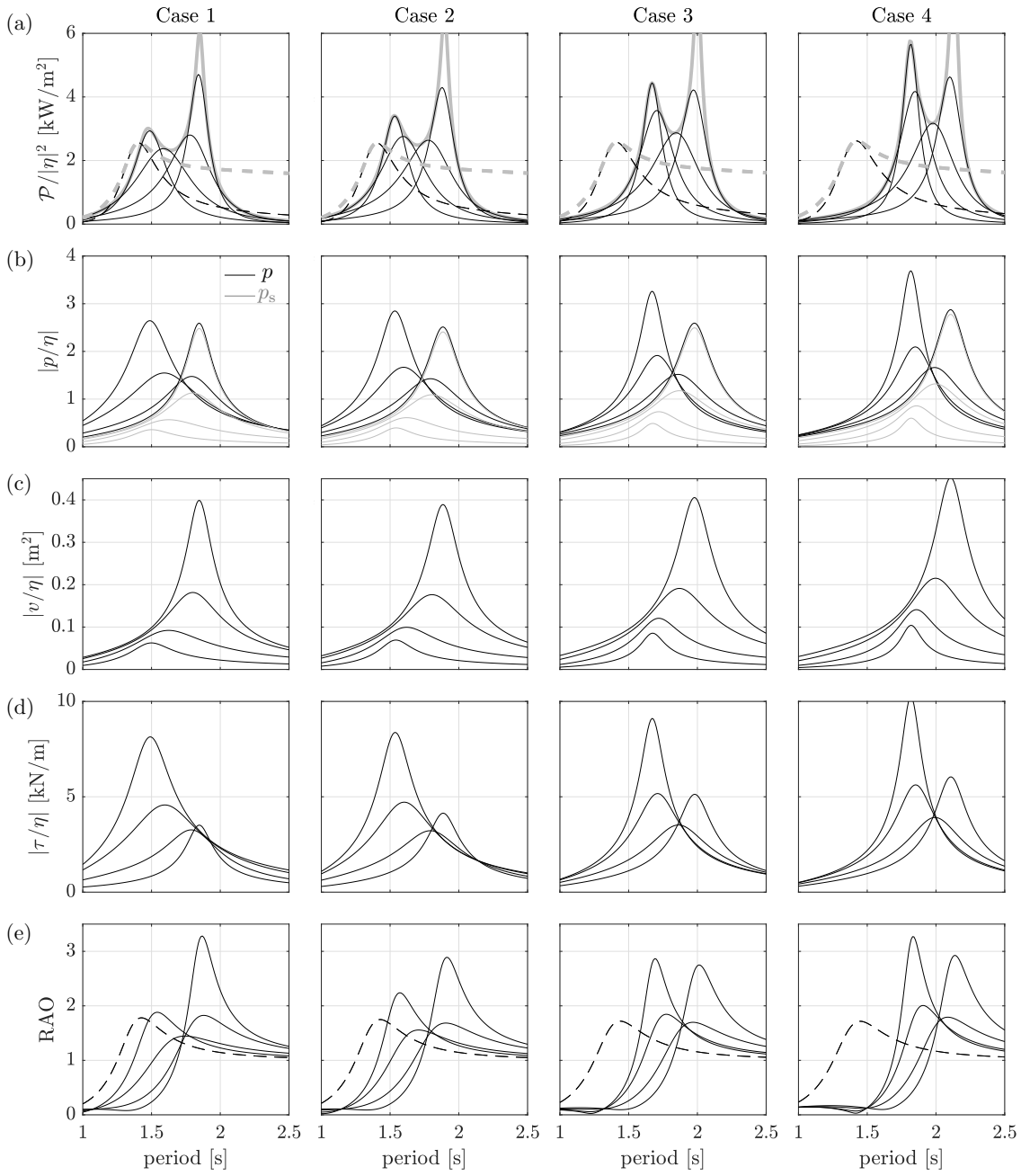

Fig. 9. (a) Power function, (b) dynamic pressure per incident wave amplitude, (c) bag volume change per incident wave amplitude, (d) tension amplitude per incident wave amplitude, and (e) response amplitude operator of the top of the bag, for Cases 1 to 4. In (a)–(e), solid lines are responses obtained with four different PTO damping values: 112.60, 42.10, 15.58, and 5.74 kPa m^{-3} s. As these values increase, so the response peaks shift from left to right. The same set of PTO damping values is used for each case. In (b), black lines are the pressure in the bag, whereas grey lines are the pressure in the secondary volume. In (a) and (e), dashed line is the response of a rigid body of the same geometry, with PTO damping selected to maximise the mean absorbed power at resonance (solid) and PTO damping optimised at every period (grey). In (a), grey thick line is the envelope of the black solid lines for all PTO coefficients (not just the four shown here).

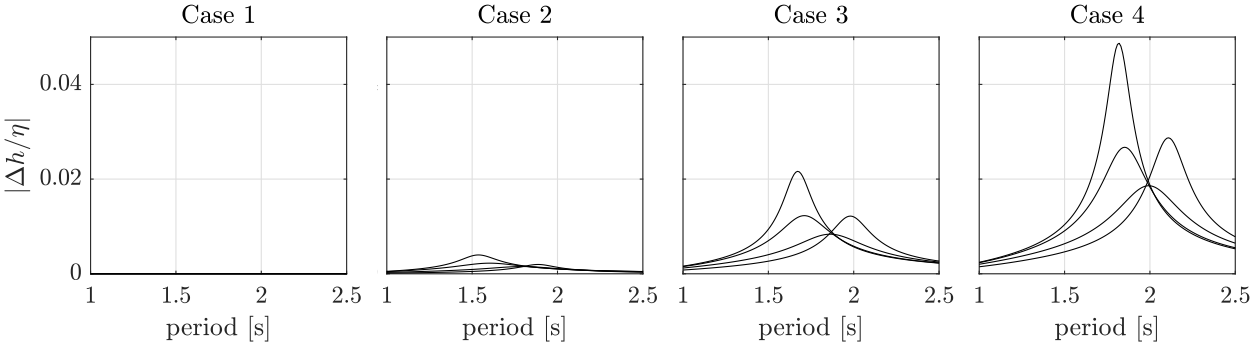

Fig. 10. Change in element length per incident wave amplitude, for Cases 1 to 4.

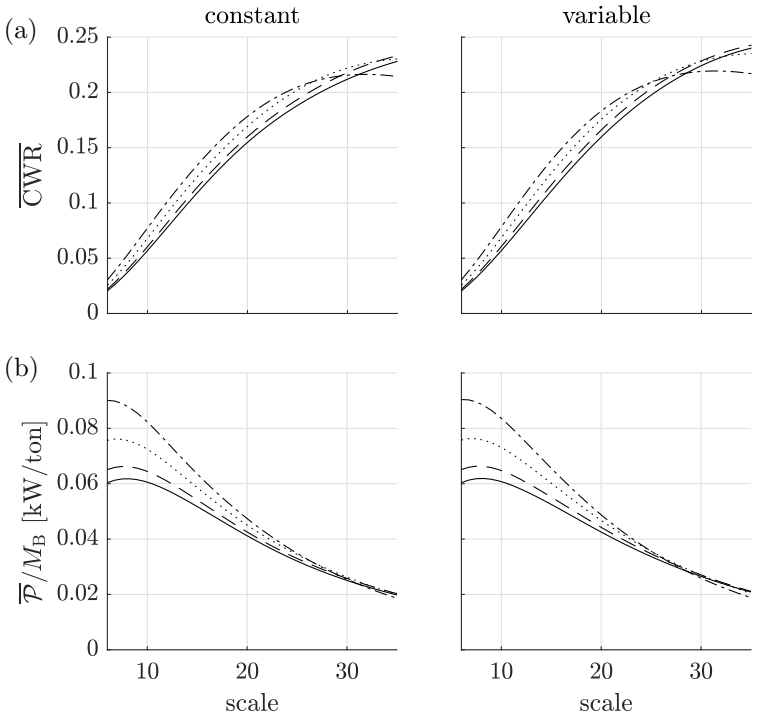

Fig. 11. (a) Mean capture width ratio and (b) mean absorbed power per unit mass (in kW/ton), plotted as functions of device scale, for the four tendon elasticity cases: Case 1 (solid), Case 2 (dashed), Case 3 (dotted), and Case 4 (dash-dotted). Left column is for constant PTO damping optimised to maximise mean absorbed power for the entire wave climate, whereas right column is for PTO damping optimised to maximise the mean absorbed power for each sea state.

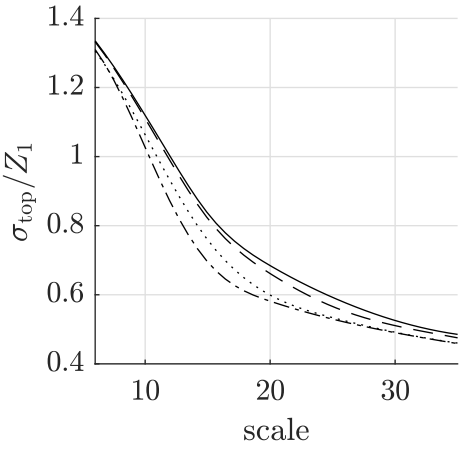

Fig. 12. Maximum standard deviation of the displacement of the bag top, normalised with the mean freeboard, for the four tendon elasticity cases: Case 1 (solid), Case 2 (dashed), Case 3 (dotted), and Case 4 (dash-dotted).